A multiscale constitutive model for the sintering of an air-plasma sprayed thermal barrier coating, and its response under hot isostatic pressing

N A Fleck [(1)] and A C F Cocks [(2)]

[(1)] Corresponding author. Cambridge University Engineering Dept., Trumpington St., Cambridge, CB2 1PZ, UK, phone: +44-1223-748240; fax +44-1223-332662; email NAF1@eng.cam.ac.uk

[(2)] Dept. of Engineering Science, Parks Rd., Oxford, OX1 3PJ, UK

4 November 2008

Summary

A micromechanical model is developed for the sintering of an air-plasma-sprayed, thermal barrier coating, and is used to make predictions of microstructure evolution under free sintering and under hot isostatic pressing. It is assumed that the splats of the coating are separated by penny-shaped cracks; the faces of these cracks progressively sinter together at contacting asperities, initially by the mechanism of plastic yield and subsequently by interfacial diffusion. Diffusion is driven by the reduction in interfacial energy at the developing contacts of the cracks and also by the local contact stress at asperities. The contact stress arises from the remote applied stress and from mechanical wedging of the rough crack surfaces. Sintering of the cracks leads to an elevation in both the macroscopic Young's modulus and thermal conductivity of the coating, and thereby leads to a degradation in thermal performance and durability. An assessment is made of the relative roles of surface energy, applied stress and crack face roughness upon the sintering response and upon the evolution of the pertinent mechanical and physical properties. The evolution in microstructure is predicted for free sintering and for hot isostatic pressing in order to provide guidance for experimental validation of the micromechanical model.

Keywords: sintering, thermal barrier coatings, variational methods, contact mechanics, creep

1. Introduction

Air plasma sprayed (APS) thermal barrier coatings (TBCs) are used extensively as protective thermal barriers of creep resistant stationary parts in land-based gas turbines. The APS coating can be deposited more cheaply and over a wider range of thickness than coatings made by electron-beam physical vapour deposition (EB-PVD). But APS coatings display a greater scatter in service life than EB-PVD coatings for reasons as yet unclear. The APS coating is deposited as liquid droplets and upon striking the substrate these droplets are rapidly solidified to pancake-shaped polycrystals, termed 'splats'. During service the splats of the APS coating sinter together at discrete contact points, giving rise to a deleterious increase in both Young's modulus and thermal conductivity, see for example Zhu and Miller (1998), Ahmaniemi *et al*. (2004), Sevostianov *et al*. (2004), Martin *et al.* (2006), Raetzer-Scheibe and Schulz (2007) and Cernuschi *et al.* (2008)). An extensive literature exists on the sintering of discrete contacts in particulate systems, see for example Cocks (1994) and Luding *et al*. (2005). The objectives of the current study are to (i) develop a physically based model of sintering of an APS coating and to (ii) explore the effect of free sintering and hot isostatic pressing (HIP) upon its mechanical properties. These preliminary calculations will be used to help steer future experiments on the sintering of APS material.

1.1 Microstructural features of the APS TBC system

The APS coating comprises an assembly of zirconia splats, with intervening cracks and porosity, as shown in Fig. 1. Typically, the TBC layer is of thickness 300-500μm, but a much wider range is achievable. The coating sits on an aluminium-rich bond coat (BC) of thickness 150-300μm. Each splat is about 1 μm thick, and has a diameter of 20-100μm. The splats have a characteristic internal microstructure: they comprise columnar grains of diameter 0.1 – 0.2μm. The inter-splat cracks are approximately penny-shaped and of diameter 20-500μm, with a maximum opening of 1μm. Initially, the highest crack density is parallel to the free surface, but these horizontal cracks sinter faster in service than other orientations (due to the negligible constraint from the underlying substrate in this direction). Porosity also exists, of volume fraction about 15% and diameter 1–20μm. The effect of voids upon the modulus and thermal conductivity is negligible, as discussed by Sevostianov *et al.* (2004).

Recall that the main function of the APS coating is to provide a thermal barrier between the hot engine gas and the underlying creep-resistant superalloy. The presence of microcracks between the splats of the coating is advantageous as they reduce the thermal conductivity of the zirconia layer. Additionally, the cracks reduce the effective Young's modulus of the coating and thereby reduce the level of in-plane thermal stress within the coating. The details are as follows. The in-plane thermal expansion coefficient of the coating, α_{TBC} = 10 x 10^{-6} K^{-1}, is significantly less than that of the underlying nickel-based superalloy, α_{Ni} = 15 x 10^{-6} K^{-1}. A sudden temperature excursion of coating and substrate will induce elastic strains within the coating, and thereby generate thermal stresses which scale with the in-plane modulus of the TBC layer. The initial in-plane modulus of the TBC layer is E_{TBC} =40GPa. This may double over the life of the coating due to sintering of the inter-splat cracks, Cernuschi *et al.* (2008). . The sintering is driven by in-plane stress within the coating and by the surface energy $\gamma_{TBC} \approx 1 Jm^{-2}$ of the zirconia on the faces of the microcracks.

1.2 Review of the deformation mechanisms for zirconia

At the operating temperature of an APS coating (1000-1300°C), the zirconia splats creep by the following argument. Each splat contains rafts of zirconia columns, of height approximately 1μm and very small diameter (about 0.1μm). Balasubramanian and Langdon (2005) have evaluated the available creep data for 3Y-TZP. They show that for a grain size of 1μm (corresponding to the height of the columnar grains of Fig 1) Coble creep dominates the material response at stress levels below about 400 MPa. We conclude that diffusion occurs relatively rapidly within the splats at engine temperature, and so the coating can be treated as a microcracked elastic, linear viscous continuum. At stresses above about 400 MPa, power law creep and plastic yield occur. To simplify the model, power law creep is neglected but ideal plasticity is included with a suitably high yield strength of σ_Y on the order of 400 MPa.

It is instructive to perform a preliminary calculation in order to determine the rate at which thermal stresses relax within the TBC coating at engine temperature. Assume that the TBC layer is in a stress-free state at the deposition temperature of T_D=500^{o}C. During operation, the peak surface temperature is taken to be T_S=1300 °C. The temperature increase of

ΔT =800 °C gives rise to a mismatch in thermal strain of $\Delta\alpha\Delta T$ = 0.4%. This mismatch is accommodated initially by tensile elastic strains (and stresses) within the TBC layer. Hence the in-plane surface stress is initially $\sigma = \sigma_i$ = 160MPa in tension.

At the simplest level, the TBC behaves as an elastic-linear viscous solid, with a modulus E in series with a dashpot of viscosity $3\eta_c$. Under fixed strain due to the substrate constraint, the in-plane stress relaxes according to

$$\sigma = \sigma_i \, exp\left(-t / \tau\right) \qquad (1)$$

where $\tau = 3\eta_c / E$ is the relaxation time constant. From the data of Balasubramanian and Langdon (2005), the uniaxial viscosity at 1300 ^{o}C is 2.5×10^{6} MPa s. Assuming an in-plane modulus E=170 GPa (from the measurements of Adams et al. (1997)) gives τ=44 s. This simple analysis suggests that the stress quickly relaxes at typical service temperatures.

The generic problem addressed below is the progressive sintering of cracks within the TBC layer. Small pores will sinter shut early in the life, while larger pores remain with negligible change in diameter. In contrast, the cracks between splats will progressively sinter at local contacting asperities, as sketched in Fig. 2. Sintering of the contacting asperities leads to a mutual approach of the crack faces and to shrinkage of the TBC coating. But the coating is constrained against shrinkage by the underlying substrate, and equi-biaxial stress is generated within the layer. In turn, Coble creep within the coating relaxes this tensile stress and thereby accelerates sintering. But in order to be more precise, it is necessary to develop a quantitative constitutive model for sintering of the APS material. This is the purpose of the present paper.

1.3 Outline of study

The APS zirconia layer is treated as a random distribution of penny-shaped cracks. The crack faces are in contact at asperities, and these contacts endow the faces of the penny-shaped cracks with a finite contact stiffness. If the contact stress on an asperity exceeds the indentation hardness at the operating temperature, then rate-independent plastic flow occurs and the contact area increases in order to carry the contact load. Diffusional flow also occurs at the asperity level and leads to an increase (or decrease) in the size of the contacts and thereby changes the contact stiffness. Simultaneously, bulk diffusional flow within the splats causes them to undergo linear viscous creep. The general problem

addressed comprises interfacial diffusion at the asperity level, along with bulk Coble creep, and elastic straining of the solid.

The variational method of Cocks, Gill and Pan (1999) is used to obtain the macroscopic constitutive law and the evolution of the microstructure in terms of crack opening v and shape of the asperities. This procedure requires a knowledge of the free energy G per unit volume of the cracked TBC, and the dissipation, expressed through a rate potential Ψ, arising from the local flux of matter. An explicit relation is derived for the dependence of G upon a set of geometric variables which describe the contact conditions. The rate potential Ψ is a convex function of the diffusion flux, of the creep-indentation rate and of the strain-rate due to Coble creep of the solid (excluding the cracks). Ψ is expressed as an explicit function of the rate of change of the geometric variables and of the bulk strain rate. For a given distribution of cracks, the rate of evolution of the microstructure minimises the functional (see Cocks *et al.*, 1999)

$$\Omega \equiv \dot{G} + \Psi \tag{2}$$

This minimisation procedure is adopted in order to obtain the governing set of constitutive relations for the solid. The multi-scale model is developed in the following sequence.

(i) In order to derive an expression for the free energy G, the elastic response of the cracked solid is obtained with the penny-shaped cracks subjected to a tensile bridging traction T.

(ii) The elastic energy associated with contact compliance at the asperity level, and the interfacial energy of the penny shaped cracks also contribute to G, and appropriate expressions for these contributions are derived.

(iii) The evolution of asperity shape is due to interfacial diffusion at the asperity level, with the initial contact size set by plastic indentation of the asperities. Geometric relations for a typical asperity are derived, and dissipation potentials are derived for the sintering of each asperity by interfacial diffusional flow.

(iv) The contributions to the overall dissipation potential are obtained for bulk Coble creep of the APS coating.

(v) The overall variational statement for the evolution of state variables is given, and the resulting system of constitutive relations is derived.

The above constitutive description is time-integrated in order to obtain the evolution of microstructure, and the accompanying evolution of macroscopic modulus and thermal conductivity for the loading case of hot isostatic pressing of the APS solid, including the special case of free sintering under zero macroscopic stress. Finally, the consequences of asperity sintering upon the effective values of Young's modulus and the thermal conductivity are determined.

2. Sintering model for an isotropic distribution of penny-shaped cracks with asperity-bridging

It is appreciated that the microcrack network is anisotropic in general, and consequently the elastic properties vary with direction. Significant progress on the elastic and thermal properties of anisotropic, cracked solids has been made recently by Kachanov and co-workers, see for example Kachanov *et al.* (2001) and Sevostianov *et al*. (2004). The current study is an attempt to develop the essential mathematical structure for multi-scale effects in the sintering of an APS coating. For clarity and insight, we limit our geometric description of the sintering process to the essentials. The aim is to explore competing mechanisms of local sintering and bulk elastic, plastic and creep deformation. Insufficient experimental data are available at this stage to justify a full anisotropic description.

2.1 The Physical Problem

The problem we consider here is shown schematically in Fig. 2 and consists of a random, isotropic distribution of penny-shaped cracks. The elastic solution to this problem has already been given by Budiansky and O'Connel (1976), and we modify their analysis to include the effect of crack bridging by contacting asperities. They considered the more general problem of a cracked solid containing *elliptical* cracks of random orientation and random size, but here we restrict attention to circular cracks. Assume that the solid contains *N penny-shaped* cracks per unit volume, of random orientation and random radius *R*. Then, Budiansky and O'Connel show that the macroscopic bulk modulus K and shear modulus μ depend upon a dimensionless 'damage parameter' $f \equiv N\left\langle R^3 \right\rangle$, where the angle brackets denote an average. For convenience, we introduce a representative radius $\overline{R} \equiv \left\langle R^3 \right\rangle^{1/3}$ of the penny-shaped cracks, and treat this as the length scale of the micro-cracked solid.

The surfaces of the cracks are assumed to be rough and in contact at the asperity level. The traction across the crack faces is quantified by a net tensile bridging stress T (negative in value when the cracks are internally pressurised by overlapping asperities).

2.2 Elastic response and the strain energy

Consider a microcracked solid as sketched in Fig. 2. The solid is loaded by a macroscopic stress state σ^{∞}, and the crack faces are subjected to a tensile normal traction T which tends to close the cracks. We make use of the Budiansky-O'Connell (1976) analysis to determine the elastic constitutive response. The solid responds with a macroscopic strain ε and the cracks possess an average opening v_{E}. First, consider the case where the cracks are open and traction-free. Then, the Young's modulus of the cracked solid E is related to the Young's modulus of the uncracked parent solid E_0 via a knock-down factor χ, such that

$$E = \chi E_0 \qquad \text{where} \qquad \chi = 1 - \frac{16}{9} f \tag{3}$$

Similarly, the Poisson's ratio ν of the cracked solid is related to the value ν_0 of the uncracked solid according to

$$\nu = \chi \nu_0 \tag{4}$$

The expressions (3) and (4) are excellent approximations to the more complicated analytic expressions given by Budiansky and O'Connell (1976). The bulk modulus K reads

$$K = \frac{E}{3(1-2\nu)} = \frac{\chi E_0}{3(1-2\chi\nu_0)} \tag{5}$$

while the shear modulus μ is

$$\mu = \frac{E}{2(1+\nu)} = \frac{\chi E_0}{2(1+\chi\nu_0)} \tag{6}$$

Consequently, the elastic volumetric strain in the cracked solid ε_{Eh} is related to the applied hydrostatic stress σ_h^{∞} by

$$\varepsilon_{Eh} = \frac{\sigma_h^{\infty}}{K} \tag{7}$$

while the elastic von Mises effective shear strain ε_{Ee} is related to the von Mises stress σ_e^∞ by

$$\varepsilon_{Ee} = \frac{\sigma_e^\infty}{3\mu} \tag{8}$$

The average elastic crack opening displacement of the traction-free crack is

$$\frac{v_E}{\overline{R}} = \frac{3}{\pi f}\frac{1-\chi}{\chi}\frac{\sigma_h^\infty}{E_0} \tag{9}$$

The above expressions are easily modified by including the contribution from crack face loading. Use of the reciprocal theorem gives directly,

$$\varepsilon_{Eh} = \frac{3}{\chi E_0}\left[(1-2\chi\nu_0)\sigma_h^\infty - (1-\chi)T\right] \tag{10}$$

and

$$\frac{v_E}{\overline{R}} = \frac{3}{\pi f}\frac{1-\chi}{\chi}\frac{\left(\sigma_h^\infty - T\right)}{E_0} \tag{11}$$

with (8) remaining unchanged. Note that the pair (10) and (11) can be inverted immediately to give

$$T = \frac{E_0}{3(1-2\nu_0)}\left[\varepsilon_{Eh} - \frac{(1-2\chi\nu_0)}{(1-\chi)}\pi f\frac{v_E}{\overline{\mathrm{R}}}\right] \tag{12}$$

and

$$\sigma_h^\infty = \frac{E_0}{3(1-2\nu_0)}\left[\varepsilon_{Eh} - \pi f\frac{v_E}{\overline{\mathrm{R}}}\right] \tag{13}$$

In order to solve the sintering problem, we shall require an expression for the elastic strain energy per unit volume *U* of the cracked solid, including the contribution from the elastic indentation of the asperities. The average crack opening displacement *v* of the bridged penny-shaped cracks comprises an elastic opening v_E and a creep opening v_C. Compatibility dictates that the total displacement $v = v_E + v_C$ equals the sum of the extra displacement due to the spring-like extension of asperities u_S, the plating of matter by sintering at the contacting asperities u_P and an initial asperity height u_1 due to wedging of one asperity against its neighbour on the opposing face, giving

$$v = v_E + v_C = u_S + u_P + u_1 \tag{14}$$

A variational method is used below in order to obtain the rate quantities $(\dot{v}_C, \dot{u}_P)$. The total strain energy of the cracked solid, including the contribution $U_S(u_S)$ from the elastic indentation of each asperity, is

$$U = \frac{1}{2}\sigma_h^\infty \varepsilon_{Eh} + \frac{1}{2}\sigma_e^\infty \varepsilon_{Ee} + \frac{\pi}{2} fT \frac{(u_S - v_E)}{\bar{R}}$$

$$= \frac{E_0 \varepsilon_{Eh}}{6(1-2\nu_0)}\left[\varepsilon_{Eh} - \pi f \frac{v_E}{\bar{R}}\right] + \frac{3}{4}\frac{\chi E_0 \varepsilon_{Ee}^2}{(1+\chi\nu_0)} \tag{15}$$
$$+ \frac{\pi f E_0}{6(1-2\nu_0)}\left[\varepsilon_{Eh} - \frac{(1-2\chi\nu_0)}{(1-\chi)}\pi f \frac{v_E}{\bar{R}}\right]\frac{(u_S - v_E)}{\bar{R}}$$

2.3 The local contact problem

In order to develop a tractable micromechanical model of the evolution of contacts, the roughness of the crack surfaces is combined into a single wavy surface while the other surface is treated as perfectly flat. Each asperity is treated as a circular conical frustum, with top diameter 2*b*, bottom diameter λ and height *w* as sketched in Fig. 3. The roughness is on the length scale of the TBC columns within each splat, with a wavelength *s*. Consequently, the ratio of true area of contact to nominal area of contact is $(2b/s)^2$. At any instant in time it is helpful to distinguish between the *relaxed configuration* in the deformed but unloaded state, and the *loaded configuration* where the conical asperities are subjected to an additional instantaneous extension of u_S associated with the traction *T*. In the relaxed configuration, the combined peak-peak amplitude of the roughness equals *w*. As interfacial diffusional flow proceeds, *w* decreases, the contact diameter 2*b* and the base diameter λ both increase and the wavelength *s* remains fixed. We note in passing that this idealisation has only a limited number of geometric variables to define the problem, yet has sufficient flexibility in order to predict the evolution of roughness shape and amplitude.

An initial reference configuration is also introduced for algebraic convenience, see Fig. 4a. This configuration defines the pre-sintered state in terms of the diameter λ_0 and height w_0. However, asperity sintering occurs during both deposition and service, and so the

reference state is not physically realised: the TBC has already partially sintered after deposition.

The problem posed is to solve for the local evolution of surface profile due to the interfacial diffusion of matter from the contacts into the gaps of peak-peak amplitude w. Interfacial diffusion is driven by the combined driving forces of the net reduction in interfacial energy, and the elastic strain energy of the TBC.

Straightforward geometrical arguments can be used to relate the contact width 2*b* and the inclination β to the primary unknowns (w, λ). Incompressibility dictates

$$2b = -\frac{\lambda}{2} + \sqrt{{\lambda_0}^2 \frac{w_0}{w} - \frac{3}{4}\lambda^2} \tag{16}$$

with

$$\tan\beta = \frac{2w}{\lambda - 2b} \tag{17}$$

and

$$\lambda^2 = w^2 + \left(\frac{\lambda}{2} - b\right)^2 \tag{18}$$

Assume an initial state after deposition such that (w_1, λ_0) are the initial values of (w, λ). Then, the compatibility statement (14) dictates that the plating displacement u_P is related to the asperity height *w* according to

$$u_P = w - w_1 \tag{19}$$

The local sintering problem

It is assumed that matter diffuses along the interface from the contacts in Fig. 5, and deposits along the free surfaces of length λ. Matter diffuses from the sides of asperities, of local surface energy γ_S to contacts with interfacial energy γ_G. These surface energies contribute to the free energy G_S of the solid. The free surface energy per asperity reads

$$G_S = \pi b^2(\gamma_G - \gamma_S) + \frac{\pi}{4}\frac{1}{\cos\beta}\left(\lambda^2 - 4b^2\right)\gamma_S - \frac{\pi}{4}\lambda^2\gamma_S \tag{20}$$

Additionally, the fixed 'dead loads' associated with a fixed macroscopic stress state σ_{ij}^{∞} contribute to *G*. The solid responds with a macroscopic strain ε_{ij} The total Gibbs free energy per unit volume *G* reads

$$G = U + \frac{4f}{\overline{R}s^2} G_S - \sigma_{ij}^{\infty} \varepsilon_{ij} \tag{21}$$

where the internal strain energy *U* has already been stated by (15). We proceed to derive an explicit relation for the contact stiffness of the asperities $k \equiv T / u_S$.

The contact stiffness of the asperities

The effective spring constant *k* for the asperities which bridge penny shaped cracks is determined as follows. We consider two extremes of topology for the asperities. First, consider small, widely spaced asperities and treat them as isolated circular junctions of radius *b* and spacing *s* bridging two parallel planes under a nominal tensile traction *T*. The tensile load $P = \pi s^2 T / 4$ is carried by each junction. The associated displacement is deduced from the solution for normal indentation of a half-space by a frictionless, rigid punch of circular section. The resulting contact stiffness k_1 is

$$k_1 = \frac{T}{u_S} = \frac{4P}{\pi s^2 u_S} = \frac{4bE'}{\pi s^2} \tag{22}$$

where $E' = E_0 / \left(1 - \nu_0{}^2\right)$. Now consider the other extreme topology where asperities bridge most of the faces of the penny-shaped cracks, with occasional 'minor' cracks existing between the asperities. These minor cracks are treated as isolated and circular, of radius *a* much smaller than their spacing *s*. The area fraction of the minor cracks on the faces of the macroscopic penny-shaped cracks of radius $\overline{R}$ follows as

$$\omega = \frac{\pi a^2}{\pi s^2 / 4} = \frac{4a^2}{s^2} \tag{23}$$

while the ligament area fraction $1 - \omega$ is

$$1 - \omega = \frac{4b^2}{s^2} \tag{24}$$

Consequently, *a/s* is given by

$$\frac{4a^2}{s^2} = 1 - \frac{4b^2}{s^2} \tag{25}$$

Now the average crack opening of a circular crack in an infinite elastic solid is

$$\delta = \frac{16}{3\pi}\frac{Ta}{E'} \tag{26}$$

and so the contact stiffness due to an area fraction ω of the minor cracks is

$$k_2 \equiv \frac{T}{u_S} = \frac{T}{\omega\delta} = \frac{3\pi E'}{8s}\left[1-\frac{4b^2}{s^2}\right]^{-3/2} \tag{27}$$

In order to proceed, an interpolation formula is needed for the effective contact stiffness *k* between the values of k_1 at small *b/s* and k_2 at *b/s* close to 1/2. We make the choice

$$T = ku_S \tag{28a}$$

where

$$k = \frac{k_1}{2}\left(1+\cos\frac{2\pi b}{s}\right)+\frac{k_2}{2}\left(1-\cos\frac{2\pi b}{s}\right) \tag{28b}$$

as this preserves the asymptotic behaviour except for mid-range values of *b/s* close to 1/4.

3. The dissipation potentials within the solid: bulk creep and contact diffusion

The local sintering problem

Fick's first law states that the interfacial flux vector $\boldsymbol{j}$ (in units of m^2s^{-1}) is related to the gradient of chemical potential μ_{chem} (Jm^{-3}) by

$$\boldsymbol{j} = -D\nabla\mu_{chem} \tag{29}$$

where *D* is the interfacial diffusivity (in units of $m^6J^{-1}s^{-1}$). *D* is temperature dependent such that

$$D = \frac{\delta\Omega}{kT}D_0\exp(-q/kT) \tag{30}$$

in terms of a reference diffusivity D_0, atomic volume Ω, interface thickness δ, thermal activation energy *q* and Boltzmann constant *k*.

Mass conservation at an interface dictates that the normal velocity of the interface $\dot{u}_n$ is related to the flux *j* according to

$$\dot{u}_n + \nabla\cdot\boldsymbol{j} = 0\ . \tag{31}$$

Next, introduce the rate potential Ψ_s for a representative single asperity. The potential Ψ_s is expressed in terms of the volumetric interfacial flux *j*; this flux is labelled j_1 and is a function of the arc length s_1 along the contact OA. Likewise, it is labelled j_2 and is a function of the arc length s_2 along the contact AB, as shown in Fig. 5. Define

$$\Psi_s = \frac{1}{D_G}\int_0^b \pi s_1 {j_1}^2 ds_1 + \frac{\cos\beta}{D_S}\int_{b/\cos\beta}^{\lambda+(b/\cos\beta)} \pi s_2 {j_2}^2 ds_2 \tag{32}$$

where (D_G, D_S) are the diffusion constants for interfacial diffusion along OA and surface diffusion along the free surface AB, respectively, as specified by (30). Now the flux $j_1(s_1)$ along OA is related directly to the rate of separation $\dot{w}$ of two contacting columns by the kinematic relation (31), giving

$$j_1 = -\frac{1}{2}\dot{w}s_1 \tag{33}$$

on OA. Similarly, the flux $j_2(s_2)$ along AB is obtained from the normal velocity of the free surface v_n, to give

$$\frac{\partial(j_2 s_2)}{\partial s_2} = -v_n s_2 \tag{34}$$

Geometry dictates that v_n can be stated in terms of $(\dot{w}, \dot{\lambda})$ according to

$$v_n = \left(\dot{w}\cos\beta + \dot{b}\sin\beta\right)\left(\frac{\lambda\cos\beta + b}{\lambda\cos\beta}\right) - \frac{\dot{\lambda}b}{2\lambda}\tan\beta - \left[\left(\dot{b} - \frac{\dot{\lambda}}{2}\right)\sin\beta + \dot{w}\cos\beta\right]\frac{s_2}{\lambda} \tag{35}$$

with $\dot{b}(\dot{w}, \dot{\lambda})$ given by the rate form of (16). Integration of (34) with (35) gives

$$j_2 = \left(\frac{A_1}{s_2} + B_1 s_2 + C_1 {s_2}^2\right)\dot{w} + \left(\frac{A_2}{s_2} + B_2 s_2 + C_2 {s_2}^2\right)\dot{\lambda} \tag{36}$$

Explicit expressions for (A_i, B_i, C_i) are given in Appendix A. The macroscopic dissipation due to sintering per unit volume of TBC Ψ_P is related to Ψ_s by

$$\Psi_P = \frac{4N\bar{R}^2}{s^2}\Psi_s \tag{37}$$

An explicit expression for Ψ_s is obtained by integration of (32), using the expressions (33) and (36) for the fluxes, to give

$$\Psi_s(\dot{w}, \dot{\lambda}) = \frac{\pi}{16}\frac{b^4}{D_G}\dot{w}^2 + \frac{\pi\cos\beta}{D_S}(\dot{w} \quad \dot{\lambda})(\boldsymbol{d})\begin{pmatrix}\dot{w}\\ \dot{\lambda}\end{pmatrix} \tag{38}$$

where $\boldsymbol{d}$ is a 2x2 matrix with components d_{ij}. These components are bi-linear in (A_i, B_i, C_i), and are listed in Appendix A. But there is an additional dissipation due to linear creep of the matrix, and this is now detailed.

Dissipation potential for bulk creep

We assume that the splats undergo Coble creep, such that the macroscopic creep rate is linear in remote stress. Consider the creep response of the micro-cracked solid shown in Fig. 4: the matrix creeps in an incompressible manner with a shear viscosity η_0, in addition to its linear elastic response. Consequently, the bridged penny-shaped cracks open at a rate $\dot{v}$, as already stated in (14). The relations stated above for the isotropic, elastic response of the solid containing penny-shaped cracks can be re-written immediately for the linear viscous solid. The usual transformation from elastic response to linear, incompressible viscous response applies for the matrix: $\varepsilon_{Eij} \to \dot{\varepsilon}_{ij}$, $E_0 \to 3\eta_0$ and $\nu_0 \to 0.5$. Assume the cracked solid is subjected to a macroscopic stress state σ^∞ and crack face closing tractions *T*. The average crack face opening rate $\dot{v}$ is then

$$\frac{\dot{v}}{\bar{R}} = \frac{1}{\pi f}\left(\frac{1-\chi}{\chi}\right)\left(\frac{\sigma_h^\infty - T}{\eta_0}\right) \tag{39}$$

The creep rate $\dot{\varepsilon}_{ij}$ is related to the macroscopic deviatoric stress $s_{ij}^\infty \equiv \sigma_{ij}^\infty - \sigma_h^\infty \delta_{ij}$ and mean stress via the isotropic relation,

$$\dot{\varepsilon}_{ij} = \frac{(2+\chi)}{6\chi\eta_0} s_{ij}^\infty + \frac{1}{3}\left(\frac{1-\chi}{\chi}\right)\frac{\left(\sigma_h^\infty - T\right)}{\eta_0}\delta_{ij} \tag{40}$$

Thus, the volumetric creep rate is

$$\dot{\varepsilon}_h = \left(\frac{1-\chi}{\chi}\right)\left(\frac{\sigma_h^\infty - T}{\eta_0}\right) = \pi f \frac{\dot{v}}{\bar{R}} \tag{41}$$

while the deviatoric creep rate is

$$\dot{\varepsilon}_e = \left(\frac{2+\chi}{9\chi}\right)\frac{\sigma_e^\infty}{\eta_0} \tag{42}$$

The total dissipation per unit volume Ψ within the solid from sintering and bulk creep follows as

$$\Psi = \Psi_P + \frac{1}{2}\sigma_h^\infty \dot{\varepsilon}_h + \frac{1}{2}\sigma_e^\infty \dot{\varepsilon}_e - \frac{\pi}{2} fT \frac{\dot{v}_C}{\bar{R}}$$

$$= \Psi_P + \frac{1}{2}\frac{\chi\eta_o}{(1-\chi)}\dot{\varepsilon}_h^2 + \frac{1}{2}\frac{9\chi\eta_o}{(2+\chi)}\dot{\varepsilon}_e^2 \tag{43}$$

We emphasise that Ψ is a quadratic function of the rates $\left(\dot{w}, \dot{\lambda}, \dot{\varepsilon}_h, \dot{\varepsilon}_e\right)$ and is needed for construction of the functional Ω in equation (2). We proceed to determine $G\left(w, \lambda, \dot{\varepsilon}_h, \dot{\varepsilon}_e\right)$ as also required by (2).

4. The variational statement, and the resulting system of constitutive relations

Consider a given state of contact of the penny-shaped cracks in the APS material, and assume a prescribed macroscopic loading σ_{ij}^∞. An examination of the above set of equations reveals that the state of the material is characterised by the instantaneous values of $\left(w, \lambda, \varepsilon_{Cij}\right)$. The cracked solid has an isotropic elastic response at the macroscopic level, with an elastic strain state ε_{Eij} specified by (8) and (10), of general form,

$$\varepsilon_{Eij} = \left(\frac{1+\nu}{E}\right)\sigma_{ij}^\infty - \frac{3\nu}{E}\sigma_h^\infty \delta_{ij} - \left(\frac{1-\chi}{\chi}\right)\frac{T}{E_0}\delta_{ij} \tag{44}$$

with (ν, E) given by (3) and (4). As usual, δ_{ij} is the Kronecker delta and repeated suffices denote summation from 1 to 3. The stress-strain relations (44) can be inverted immediately to obtain

$$\sigma_{ij}^\infty = \left(\frac{\chi}{1+\chi\nu_0}\right)E_0\varepsilon_{Eij} + \left(\frac{\chi^2\nu_0}{(1+\chi\nu_0)(1-2\chi\nu_0)}\right)E_0\varepsilon_{Ekk}\delta_{ij} + \left(\frac{1-\chi}{1-2\chi\nu_0}\right)T\delta_{ij} \tag{45}$$

The bridging traction T at any instant is obtained by substitution of (11), (19) and (28) into the compatibility statement (14), to give

$$\frac{T}{E_1} = \left(\frac{\bar{R}k}{\bar{R}k + E_1}\right)\left(\frac{\sigma_h^\infty}{E_1} + \frac{v_C + w_1 - u_1 - w}{\bar{R}}\right) \tag{46}$$

where

$$E_1 \equiv \frac{\pi}{3}\frac{\chi f}{1-\chi}E_0 \tag{47}$$

The creep component of the crack opening v_C can be expressed in terms of the volumetric creep rate by integrating (41) to obtain

$$v_C = \frac{\overline{R}}{\pi f}\varepsilon_{Ch} \tag{48}$$

Thus, the macroscopic elastic strain ε_{Eij} is known in terms of the applied stress σ_{ij}^{∞} and of current state via (44) and (46). It remains to determine how the state of the material evolves. The rate of change of the kinematic variables $(w, \lambda, \varepsilon_{Cij})$ are determined by minimising the functional $\Omega \equiv \dot{G} + \Psi$ as stated in equation (2). We proceed to evaluate the time rate of change of Gibbs free energy $\dot{G}$. Now $\dot{G}$ is linear in $(\dot{w}, \dot{\lambda}, \dot{\varepsilon}_{Cij})$ and time differentiation of (21) provides

$$\dot{G} = \frac{4f}{\overline{R}s^2}\dot{G}_S - \frac{\pi f T}{\overline{R}}\dot{w} - \left(\sigma_h^{\infty} - T\right)\dot{\varepsilon}_{Ch} - \sigma_e^{\infty}\dot{\varepsilon}_{Ce} + \frac{\pi}{2}\frac{f}{\overline{R}k^2}T^2\frac{\partial k}{\partial b}\left(\frac{\partial b}{\partial \lambda}\dot{\lambda} + \frac{\partial b}{\partial w}\dot{w}\right) \tag{49}$$

where

$$\dot{G}_S = -F_1\dot{w} - F_2\dot{\lambda} \tag{50}$$

Explicit expressions for the thermodynamic driving forces (F_1, F_2) are given in Appendix A. The partial derivatives $\left(\frac{\partial k}{\partial b}, \frac{\partial b}{\partial w}, \frac{\partial b}{\partial \lambda}\right)$ follow immediately from differentiation of (16) and (28) and are omitted here.

The optimal choice of $(\dot{w}, \dot{\lambda}, \dot{\varepsilon}_{Cij})$ is obtained by taking $\delta\Omega = \delta\dot{G} + \delta\Psi = 0$ for arbitrary variations in $(\dot{w}, \dot{\lambda}, \dot{\varepsilon}_{Cij})$. The first variation of $\dot{G}$ is obtained from (49) while $\delta\Psi$ is obtained from (43). Upon writing $\delta\Omega = 0$ we directly recover the constitutive relationships of (41) and (42) for the creep strain rates and we are left with two simultaneous equations for $(\dot{w}, \dot{\lambda})$,

$$\frac{\partial \dot{G}}{\partial \dot{w}} + \frac{\partial \Psi}{\partial \dot{w}} = 0 \tag{51}$$

and

$$\frac{\partial \dot{G}}{\partial \dot{\lambda}} + \frac{\partial \Psi}{\partial \dot{\lambda}} = 0 \tag{52}$$

Recall that $\dot{G}$ is linear and Ψ is quadratic in the rates $(\dot{w}, \dot{\lambda})$. The relations (50) and (51) can thereby be expressed in matrix form as

$$\begin{pmatrix} \dfrac{\partial^2 \Psi}{\partial \dot{w}^2} & \dfrac{\partial^2 \Psi}{\partial \dot{w} \partial \dot{\lambda}} \\ \dfrac{\partial^2 \Psi}{\partial \dot{w} \partial \dot{\lambda}} & \dfrac{\partial^2 \Psi}{\partial \dot{\lambda}^2} \end{pmatrix} \begin{pmatrix} \ddot{w} \\ \ddot{\lambda} \end{pmatrix} = - \begin{pmatrix} \dfrac{\partial \dot{G}}{\partial \dot{w}} \\ \dfrac{\partial \dot{G}}{\partial \dot{\lambda}} \end{pmatrix} \tag{53}$$

This can be inverted algebraically to obtain $(\ddot{w}, \ddot{\lambda})$ as a function of the current state (w, λ, v_C). The time evolution of (w, λ) follows by integration using any convenient scheme.

The set of constitutive relations are now complete. At any given state, the macroscopic elastic strain is specified by (44), in terms of the bridging traction *T* as given by (46). The macroscopic creep strain rate and the rate of crack opening due to creep deformation are obtained from (40) and (39), while the contact geometry evolves according to (52). The plating displacement across the faces of the penny-shaped cracks is given by (19).

5. Prediction of the response under Hot Isostatic Pressing

It is instructive to predict the hot isostatic pressing (HIP) response of the APS TBC using the above constitutive relations. Consider the problem of heating the APS ceramic to a sufficiently high temperature (say 1000°C) and then applying a fixed pressure $p^\infty = -\sigma_h^\infty$ so that the ceramic undergoes bulk creep and simultaneous sintering of the penny-shaped cracks. The evolution of the asperity size can be predicted, along with the change in macroscopic modulus of the coating. We proceed to specialize the constitutive relations to the HIP problem.

The initial state

The initial value of radius *b* of the asperities is determined by the initial value of compressive traction $|T|$ bridging the cracks. Assume that the indentation pressure at each asperity is $3\sigma_Y$. Then, equilibrium dictates that the initial radius is

$$b = \frac{s}{2}\left(\frac{|T|}{3\sigma_Y}\right)^{1/2} \tag{54}$$

The initial height of asperity $w(t=0) \equiv w_1$ follows immediately from (16) as

$$w_1 = w_0 {\lambda_0}^2 \left[\frac{3}{4} {\lambda_0}^2 + \left(2b + \frac{\lambda_0}{2} \right)^2 \right]^{-1} \tag{55}$$

It remains to obtain the initial asperity height u_1 associated with asperity wedging. Substitution of (11) and (28a) into the compatibility statement (14) gives

$$u_1 = v_E - u_S = -\frac{3}{\pi f} \left(\frac{1-\chi}{\chi} \right) \left(\frac{p^\infty + T}{E_0} \right) - \frac{T}{k} \tag{56}$$

The numerical scheme

The rate of accumulation of hydrostatic creep strain $\dot{\varepsilon}_{Ch}$ and of crack opening $\dot{v}_C$ are specified by (41). Also, the rates $(\dot{w}, \dot{\lambda})$, governing asperity evolution, are specified by (52). Note that the rates $(\dot{w}, \dot{\lambda}, \dot{v}_C)$ form a coupled set, and depend upon the current values of (w, λ, v_C). This set of equations is integrated using a fourth order Runge-Kutta scheme.

Sintering leads to an increase in the contact stiffness k and thereby to a progressive increase in macroscopic bulk modulus, but not shear modulus. The elastic hydrostatic strain ε_{Eh} at any instant in time, under a fixed macroscopic pressure $p^\infty = -\sigma_h^\infty$, follows directly from (10), with the traction T specified by (46). Consequently, the effective bulk modulus K_{eff} is given by

$$\frac{1}{K_{eff}} \equiv \frac{d\varepsilon_{Eh}}{d\sigma_h^\infty} = \frac{1}{K} - \frac{3(1-\chi)}{\chi E_0} \frac{Rk}{E_1 + Rk} \tag{57}$$

Recall that K is the bulk modulus of the Budiansky-O'Connell solution for a solid containing unbridged penny-shaped cracks specified by (5) and E_1 is given by (47). The shear modulus μ is given by (6), the effective Poisson's ratio is

$$\nu_{eff} = \frac{3K_{eff} - 2\mu}{2(3K_{eff} + \mu)} \tag{58}$$

and the effective Young's modulus is

$$E_{eff} = 3K_{eff}(1 - 2\nu_{eff}) \tag{59}$$

Non-dimensionalisation of the problem

Before presentation of the results, the problem is non-dimensionalised in order to minimize the number of independent variables. All length scales are normalized by the initial asperity base diameter λ_0, such that

$$\overline{w} = \frac{w}{\lambda_0}, \quad \overline{\lambda} = \frac{\lambda}{\lambda_0}, \quad \overline{v}_C = \frac{v_C}{\lambda_0}, \quad \overline{b} = \frac{b}{\lambda_0}, \quad \overline{s} = \frac{s}{\lambda_0}, \quad \hat{R} = \frac{\overline{R}}{\lambda_0} \tag{60}$$

The appropriate non-dimensional time scale is

$$\bar{t} = \frac{E_0 t}{\eta_0} \tag{61}$$

and the non-dimensional material properties are

$$\overline{D}_G = \frac{\eta_0 \gamma_G D_G}{{\lambda_0}^4 E_0}, \quad \overline{D}_S = \frac{\eta_0 \gamma_S D_S}{{\lambda_0}^4 E_0}, \quad \overline{\gamma}_S = \frac{\gamma_S}{\gamma_G}, \quad \overline{E} = \frac{E_0 \lambda_0}{\gamma_G}, \quad \overline{\sigma}_Y = \frac{\sigma_Y \lambda_0}{\gamma_G} \tag{62}$$

All stress quantities are normalised by λ_0 / γ_G such that

$$\overline{p} = \frac{p^{\infty} \lambda_0}{\gamma_G}, \quad \overline{T} = \frac{T \lambda_0}{\gamma_G}, \quad \overline{K} = \frac{K_{eff} \lambda_0}{\gamma_G} \tag{63}$$

Typical Response

Limited data are available from the literature in order to fully specify the roughness of the microcracks in an APS coating. Unless otherwise stated, we assume that the geometry is specified by $\overline{R}$ =100 μm, s=5 μm, λ_0 =1 μm, w_0 =0.5 μm and f=0.43, and that the pertinent material properties at 1300°C are given by E_0 =170 GPa, σ_Y =400 MPa, η_0 =800 GPa s, $D_S = D_G = 6.3\text{x}10^{-31}$ $\text{m}^6\text{J}^{-1}\text{s}^{-1}$, γ_S =1 Jm^{-2} and γ_G =0.64 Jm^{-2}, taken from Brown and Ashby (1980), Swinkels and Ashby (1981), Adams et al. (1997) and Balasubramanian and Langdon (2005). The value of f=0.43 has been chosen in order to give an initial value for the Young's modulus of the APS material of 40 GPa. The initial compressive traction across the cracks is taken to be T = -5 MPa. Consequently, the non-dimensional material properties read: $\hat{R} = 100$, $\overline{s} = 5$, $\overline{w}_0$ =0.5, $\overline{\sigma}_Y = 625$, $\overline{T}$ = -7.8, $\overline{D}_G$ = $1.9\text{x}10^{-6}$, $\overline{D}_S = 3.0\text{x}10^{-6}$, $\overline{\gamma}_S$ =1.56, $\overline{E}$ =2.66 x 10^5 and $\nu = 0.3$.

The time evolution of contact geometry and bulk modulus $\left(\overline{w}, \overline{\lambda}, \overline{v}_C, \overline{b}, \overline{K}\right)$ is plotted in Fig. 6 for the choice $\overline{p} = 100$. The simulation has been run to the completion of sintering such that b attains the value of s/2, giving $\overline{b} = 2.5$. Progressive sintering leads to an

almost doubling of the non-dimensional, effective bulk modulus $\overline{K}$. The simulation reveals that the asperity shape quickly evolves from a conical frustum into a circular cylinder such that $2b = \lambda$ and $\beta = 90^{\circ}$. Thereafter, the asperities increase in diameter until they coalesce at $2b = s$. The evolution law for the circular cylinder involves only a single degree of freedom $\dot{w}$ rather than the two degrees of freedom $(\dot{w}, \dot{\lambda})$ in (53), and this leads to a simplification of the governing constitutive relations; the details are omitted here as the manipulations are routine. In order to help interpret the simulations, it is instructive to identify the competing time-scales inherent in the model.

1. $\tau_1 = \eta_0 / E_0$ is the *time constant* for creep relaxation of the uncracked solid. Consider the micro-cracked solid with initial asperity-wedging and a compressive traction across them. Then, in the absence of diffusion at the asperities, this traction is relaxed over a period on the order of τ_1. The time constant τ_1 has been used to non-dimensionalise time in (61). An initial transient in $\overline{T}$ is evident in Fig. 6 for $\bar{t} = t / \tau_1$ between 0 and 2, followed by a progressive drop in $\overline{T}$. ($\overline{T}$ remains finite in order to drive the diffusional flow at asperities).

2. The *characteristic time* for closure of the penny-shaped cracks by Coble creep is $\tau_2 = \lambda_0 \eta_0 / (\overline{R} p)$. We note that $\tau_2 / \tau_1 = \lambda_0 E / (\overline{R} p) = \overline{E} / (\hat{R} \overline{p})$ is the ratio of the characteristic time for crack closure (by Coble creep) and the time constant for stress relaxation by Coble creep. This ratio does not depend upon any creep or diffusional parameters, and can be interpreted as the ratio of asperity size (scaling with λ_0) to the magnitude of elastic opening penny-shaped cracks (scaling with $p\overline{R} / E$). A value of $\tau_2 / \tau_1 \approx 27$ is in the practical range and indicates that asperity sintering can not be accommodated simply by elastic closure of the penny-shaped cracks. We note from Fig. 6 that the time for full sintering is $\bar{t} \equiv t / \tau_1 = 23$, and this implies that the sintering time is close to τ_2.

3. The *characteristic time* for closure of the penny-shaped cracks by diffusional flow on the asperity scale is $\tau_3 = \lambda_0^{\,5} / (s^2 D_G p)$, by the following argument. The average

pressure on the top of each asperity scales as ps^2/λ_0^2, and this generates a flux of order $j = D_G ps^2/\lambda_0^3$, and a reduction rate of asperity height of order $\dot{w} = j/\lambda_0 = D_G ps^2/\lambda_0^4$. The asperities have an initial height of order λ_0, and so the relaxation time is approximately $\tau_3 = \lambda_0/\dot{w} = \lambda_0^5/\left(s^2 D_G p\right)$. Recall from equation (14) that the opening of the penny shape cracks must be compatible with the asperity height, and so the rate of sintering is dictated by the *slower* of the two rate processes of bulk creep and of diffusional flow at the asperity level. The relative rate is parameterised by the ratio $\tau_3/\tau_2 = \bar{R}\lambda_0^4/\left(s^2\eta_0 D_G\right)$. Upon substituting for the above values we find that $\tau_3/\tau_2 = 7.9$, implying that diffusion at the asperity level dictates the sintering rate. The sensitivity of sintering rate to τ_3/τ_2 is explored more fully below.

It is instructive to compare the predictions given in Fig. 6 with the free sintering response ($\bar{p} = 0$), as shown in Fig. 7. All other parameters are unchanged. Again, the simulation has been run to full sintering, $\bar{b} \to 2.5$. The qualitative response is similar in the two cases, but the timescale for pressureless sintering is much longer than for the HIP case. In both examples, there is an initial relaxation of the crack-face traction *T* and a concomitant increase in contact size *b* and in effective bulk modulus. After the initial transient, the predicted response is independent of the initial choice of *T*. For the HIP case, *T* remains compressive, but is always much smaller than the applied pressure. This reflects the fact that asperity flattening due to diffusion must be accommodated by closure of the cracks by Coble creep, which requires *T* to be smaller than *p* (see (39)). For pressureless sintering, a small tensile value of *T* is generated to close the cracks at a rate that is compatible with sintering of the asperities. Finally, the initial phase of asperity shape evolution from a conical frustum into a circular cylinder is a larger fraction of the sintering time for the case of pressureless sintering than for the HIP case.

The sensitivity of the sintering rate to the applied pressure is shown in Fig. 8. A value of $\bar{p}$ = 100 would be typical for a HIP experiment, while $\bar{p}$ = 1 is more representative of the pressure level within a TBC thin film, constrained on a substrate, as detailed below. As $\bar{p}$ is decreased from 100 to 1, the qualitative response is unchanged but the sintering time

increases by a factor of about 20. We note that τ_2 and τ_3 scale with 1/*p* and so a drop in $\bar{p}$ by a factor of 100 will lead to an increase in τ_2 and τ_3 by the same factor.

The role of $\tau_3/\tau_2 = \bar{R}\lambda_0{}^4/\left(s^2\eta_0 D_G\right)$ upon the sintering response is assessed in Fig. 9: the sintering rate is plotted against $\bar{t}$ for selected values of τ_3/τ_2 by varying D_G, with $\bar{p}$=0 and 100. (The time constant τ_1 is held fixed in these simulations.) When τ_3/τ_2 is less than about unity, the sintering rate is dictated by the characteristic time τ_2 for crack closure by Coble creep, and this time is independent of the magnitude of D_G. In contrast, when τ_3/τ_2 is greater than about unity, the sintering rate is controlled by the characteristic time τ_3 for diffusional flow at asperities.

Implications for thermal barrier coatings

The current study is limited to the simple stress state of hot isostatic pressing in order to reveal the main physical features of the sintering process and the interaction between sintering at the asperity level and bulk creep. The analysis and results presented above motivate a critical set of HIP experiments on free standing APS material. The accuracy of the model will be determined by comparison with macroscopic measurements of the modulus and thermal conductivity and microstructural measurements of asperity evolution.

Practical thermal barrier coatings are bonded to a thick substrate which constrains the in-plane deformation. An equi-biaxial state of stress σ is generated with hydrostatic component $2\sigma/3$. At engine temperature creep relaxation occurs over a time-scale of seconds, as discussed in section 1.2. The steady state stress (after relaxation) is on the order of γ_S/λ. It is concluded that a HIP study done at low pressures (including the free sintering case) will give rise to stress levels and timescales which are close to those in a practical TBC system. And now a note of caution. It is appreciated that the stress state in a HIP test is different from that in a constrained thin film, and consequently the quantitative evolution of microstructure will differ. This will be the subject of a future publication.

6. **Effect of crack density upon thermal conductivity**

In this section we make use of established cross-property relations between the effective modulus and thermal conductivity of a cracked solid in order to estimate the effect of the asperity-bridged microcracks within the APS solid upon its thermal conductivity. The cross-property relations have been obtained for mechanically open and thermally insulating cracks, and give the effective thermal conductivity in terms of the effective modulus: the crack density *f* does not appear in the relations.

Hoenig (1978, 1983) has obtained an expression for the effective thermal conductivity k_T of an isotropic conducting solid, containing a random distribution of circular, penny-shaped cracks. Let *f* denote the crack density, as above, and write k_{T0} as the thermal conductivity of the solid absent any cracks. Then, for the case of insulating cracks, he shows that

$$\frac{k_T}{k_{T0}} = 1 - \frac{8}{9} f \tag{64}$$

Compare this expression with the self-consistent expression (3) for the Young's modulus of unbridged penny-shaped cracks. Upon elimination of *f* these two expressions can be re-written as

$$\frac{k_{T0} - k_T}{k_{T0}} = \frac{1}{2} \frac{E_0 - E}{E_0} \tag{65}$$

We argue that the effect of crack-bridging by asperities is to modify to the same degree the effective value of crack density *f* in the expressions for the macroscopic modulus (3) and thermal conductivity (64). Consequently, the cross-property correlation (65) remains useful for the case of bridged cracks. It shows that thermal conductivity is less sensitive to the presence of cracks than the Young's modulus of the solid.

Likewise, Sevostianov et al (2004) have determined cross-property relations for an isotropic distribution of traction-free cracks. They obtain

$$\frac{k_{T0} - k_T}{k_T} = \frac{1}{2.14} \frac{E_0 - E}{E} \tag{66}$$

which is in close agreement with (65) for a low crack density.

It remains to make the case that heat conduction can be neglected across the unbridged portion of the crack faces. In general, we might expect that the effective thermal

conductivity of a microcracked body depends upon the conductivity of the gas within the microcracks and upon the rate of thermal radiation across the cracks. However, Lu et al (2001) have shown that both paths of heat conduction are negligible in comparison with thermal conduction through the ceramic.

7. Concluding Remarks

The constitutive model developed in this study is based upon our current understanding of the dominant diffusional flow processes within an APS coating, and takes into consideration the change in effective modulus that accompanies sintering. It is fully recognised that the dominant sintering mechanisms are dependent upon the temperature and pressure levels, with phase transformations potentially becoming significant at temperatures above 1300^{o}C. In order to build confidence in the model it is necessary to compare its predictions with sintering data. Of particular interest is the relationship between the degree of sintering, the effective modulus and the effective thermal conductivity. Detailed microstructural studies are required to confirm that the main sintering event is the bridging of cracks between splats. Clearly, these are all topics for further study.

Acknowledgements

The authors are grateful for financial support from the US Office of Naval Research (grant number N00014-05-1-0376, contract monitor Dr. David Shifler) and to the EPSRC (grant number EP/C52392X/01). Technical discussions with Drs. Stefan Lampenscherf and Harald Harders of Siemens AG are much appreciated.

References

Adams, J.W., Ruh, R. and Mazdiyasni, K.S. (1997). *J. Eur. Ceramics Soc.*, **80**, 903-908.

Ahmaniemi, S., Vuoriato, P., Mantyla, T., Cernuschi, F. And Lorenzoni, L. (2004). *J. Eur. Ceramics Soc.*, **24**, 2669-2679.

Balasubramanian, N. and Langdon, TG (2005). *Materials Science and Engineering* **A409**. pp 46-51.

Brown, A.M. and Ashby, M.F. (1980). *Acta Metallurgica*, **28**, 1085-1101.

Budiansky B and O'Connel RJ (1976). *Int Jnl Solids Structures*, **12**, pp81-97.

Cernuschi, F., Bison, P.G., Marinetti, S. and Scardi, P. (2008). Thermophysical, mechanical and microstructural characterization of aged free-standing plasma-sprayed zirconia coatings. *Acta Materialia*, **56**, 4477-4488.

Cocks, A.C.F. (1994). The structure of constitutive laws for the sintering of fine-grained materials. *Acta Metall.*, **42**, 2191-2210.

Cocks, A.C.F., Gill, S.P.A. and Pan, J. (1999). *Advances in Applied Mechanics*, ed. Van der Giessen, E. and Wu, T.Y. **36**, 82-162.

Hoenig, A. (1978). *Pageoph.*, **117**, 690-710.

Hoenig, A. (1983). *J. Composite Mats.*, **17**, 231-237.

Hutchinson, R.G., Fleck, N.A. and Cocks, A.C.F. (2006). *Acta Mat.*, **54**, 1297-1306.

Kachanov, M., Sevostianov, I. and Shafiro, B. (2001). *J. Mech. Phys. Solids*, **49**, 1-25.

Lu, T-J, Levi, C.G., Wadley, H.N.G and Evans, A.G. (2001) Distributed porosity as a control parameter for oxide thermal barriers made by physical vapour deposition, *J. Am. Ceram. Soc.*, **84**, 2937-46.

Martin, C.L., Schneider, L.C.R., Olmos, L. and Bouvard, D. (2006). Discrete element modeling of metallic powder sintering. *Scripta Mat.*, **55**, 425-428.

Raetzer-Scheibe and Schulz, U. (2007). The effects of heat treatment and gas atmosphere on the thermal conductivity of APS and EB-PVD PYSZ thermal barrier coatings. *Surface and Coatings Technol.*, **201**, 7880-7888.

Sevostianov, I., Kachanov, M., Ruud, J., Lorraine, P. and Dubois, M. (2004). *Mat Sci and Engineering*, **A386**, 164-174.

Swinkels, F. B. and Ashby, M.F. (1981). *Acta Metall.*, **29**, 259-281.

Zhu, D. and Miller, R.A. (1998). *Surf. Coat. Technology*, **108-109**, 114-120.

Appendix A

Explicit expressions for (A_i, B_i, C_i) in (36) are given as follows.

$$A_1 = -\frac{b^2}{2\cos\beta} + \frac{b^2}{\lambda\cos\beta}\left[\frac{b}{6\cos\beta} + \frac{\lambda}{2}\right] - \frac{b^2\lambda_0{}^2 w_0 \sin\beta}{4\lambda w^2\cos^2\beta}\left[\frac{b}{6\cos\beta} + \frac{\lambda}{2}\right]\left[\frac{\lambda_0{}^2 w_0}{w} - \frac{3\lambda^2}{4}\right]^{-1/2}$$

$$A_2 = -\frac{b^2\sin\beta}{4\lambda\cos^2\beta}\left\{1 + \frac{3\lambda}{2}\left[\frac{\lambda_0{}^2 w_0}{w} - \frac{3\lambda^2}{4}\right]^{-1/2}\right\}\left[\frac{b}{6\cos\beta} + \frac{\lambda}{2}\right] - \frac{b^3\sin\beta}{12\lambda\cos^3\beta}$$

$$B_1 = -\frac{1}{2\lambda}\left[\lambda + \frac{b}{\cos\beta}\right]\left\{\cos\beta - \frac{\lambda_0{}^2 w_0 \sin\beta}{4w^2}\left[\frac{\lambda_0{}^2 w_0}{w} - \frac{3\lambda^2}{4}\right]^{-1/2}\right\}$$

$$B_2 = \frac{\sin\beta}{8\lambda}\left[\lambda + \frac{b}{\cos\beta}\right]\left\{1 + \frac{3\lambda}{2}\left[\frac{\lambda_0{}^2 w_0}{w} - \frac{3\lambda^2}{4}\right]^{-1/2}\right\} + \frac{b}{4\lambda}\tan\beta$$

$$C_1 = -\frac{\lambda_0{}^2 w_0 \sin\beta}{12\lambda w^2}\left[\frac{\lambda_0{}^2 w_0}{w} - \frac{3\lambda^2}{4}\right]^{-1/2} + \frac{\cos\beta}{3\lambda}$$

$$C_2 = -\frac{\sin\beta}{4\lambda}\left\{1 + \frac{\lambda}{2}\left[\frac{\lambda_0{}^2 w_0}{w} - \frac{3\lambda^2}{4}\right]^{-1/2}\right\} \qquad \text{(A1)}$$

The 2x2 components d_{ij} in (38) are bi-linear in (A_i, B_i, C_i) and are given by

$$\begin{aligned} d_{ij} = {} & A_i A_j \ln\left(1 + \frac{\lambda\cos\beta}{b}\right) + \frac{1}{2}\left(A_i B_j + A_j B_i\right)\left[\left(\lambda + \frac{b}{\cos\beta}\right)^2 - \left(\frac{b}{\cos\beta}\right)^2\right] \\ & + \frac{1}{3}\left(A_i C_j + A_j C_i\right)\left[\left(\lambda + \frac{b}{\cos\beta}\right)^3 - \left(\frac{b}{\cos\beta}\right)^3\right] + \frac{1}{4} B_i B_j\left[\left(\lambda + \frac{b}{\cos\beta}\right)^4 - \left(\frac{b}{\cos\beta}\right)^4\right] \\ & + \frac{1}{5}\left(B_i C_j + B_j C_i\right)\left[\left(\lambda + \frac{b}{\cos\beta}\right)^5 - \left(\frac{b}{\cos\beta}\right)^5\right] + \frac{1}{6} C_i C_j\left[\left(\lambda + \frac{b}{\cos\beta}\right)^6 - \left(\frac{b}{\cos\beta}\right)^6\right] \end{aligned} \qquad \text{(A2)}$$

Explicit expressions for the thermodynamic forces in (50) are

$$F_1 = \frac{\pi b\lambda_0{}^2 w_0}{2w^2}\left(\frac{\lambda_0{}^2 w_0}{w} - \frac{3\lambda^2}{4}\right)^{-1/2}\left[\gamma_G - \gamma_S\left(\frac{1+\cos\beta}{\cos\beta}\right)\right]$$

$$-\frac{\pi(\lambda+2b)\gamma_S \sin\beta}{2}\left[1-\frac{{\lambda_0}^2 w_0}{2(\lambda-2b)w}\left(\frac{{\lambda_0}^2 w_0}{w}-\frac{3\lambda^2}{4}\right)^{-1/2}\right] \tag{A3}$$

and

$$F_2=\frac{\pi b}{2}\left[1+\frac{3\lambda}{2}\left(\frac{{\lambda_0}^2 w_0}{w}-\frac{3\lambda^2}{4}\right)^{-1/2}\right]\left[\gamma_G-\gamma_S\left(\frac{1+\cos\beta}{\cos\beta}\right)\right]$$
$$+\frac{3\pi w(\lambda+2b)\gamma_S \sin\beta}{4(\lambda-2b)}\left[1+\frac{\lambda}{2}\left(\frac{{\lambda_0}^2 w_0}{w}-\frac{3\lambda^2}{4}\right)^{-1/2}\right]-\frac{\pi\gamma_S\lambda}{2}\left(\frac{1-\cos\beta}{\cos\beta}\right) \tag{A4}$$

Figure captions

Fig. 1. Main features of an APS coating. (Courtesy of S. Lampenscherf.)

Fig. 2. The microcracked geometry under study. The matrix surrounding the penny-shaped cracks is elastic, linear viscous. A tensile traction *T* pulls the faces of each crack together, under the assumed sign convention. This tensile traction stretches the bridging asperities across the crack faces, as illustrated in the intermediate figure. The lower figure details the partitioning of crack bridging displacements into elastic and plating (sintering) components.

Fig. 3. Idealisation of the surface roughness on the surface of each penny shaped crack. The roughness is represented by a random distribution of conical frusta.

Fig. 4. The local contact geometry at asperities on the surfaces of a penny shaped crack. (a) reference configuration; (b) typical state; (c) late stage of sintering.

Fig. 5. Definition of fluxes, surface energies and diffusivities at the contacts.

Fig. 6. HIP response for a constant applied pressure of $\overline{p} = 100$.

Fig. 7. Pressureless sintering response, $\overline{p} = 0$.

Fig. 8. Sensitivity of sintering rate and effective bulk modulus to the pressure. The open circles on the $\overline{b}$ -curves denote the point where the asperity shape has evolved from a conical frustum to a circular cylinder.

Fig. 9 Sensitivity of sintering response to τ_3 / τ_2, for $\overline{p}$ = 0, 100.

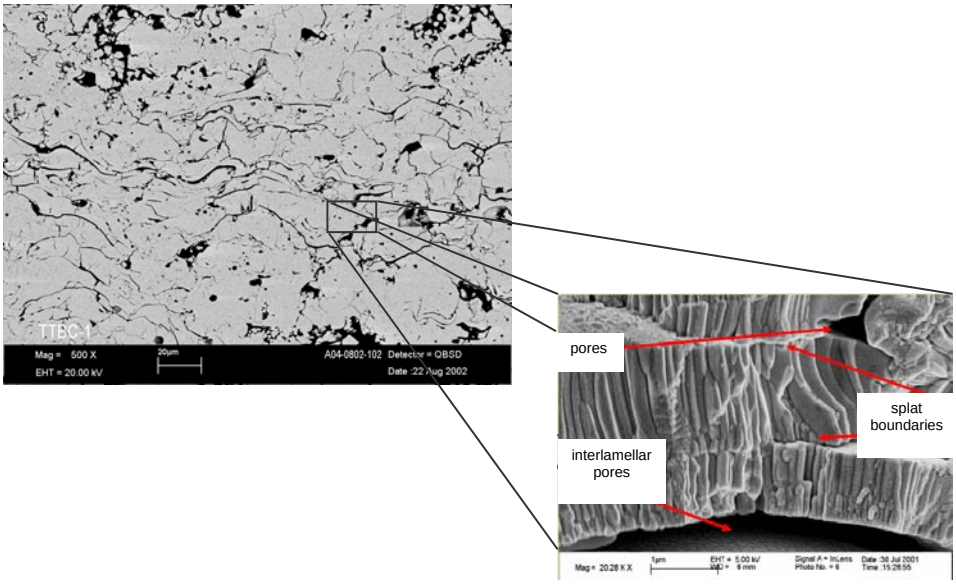

Fig. 1 Main features of the APS coating. (Courtesy of S. Lampenscherf.)

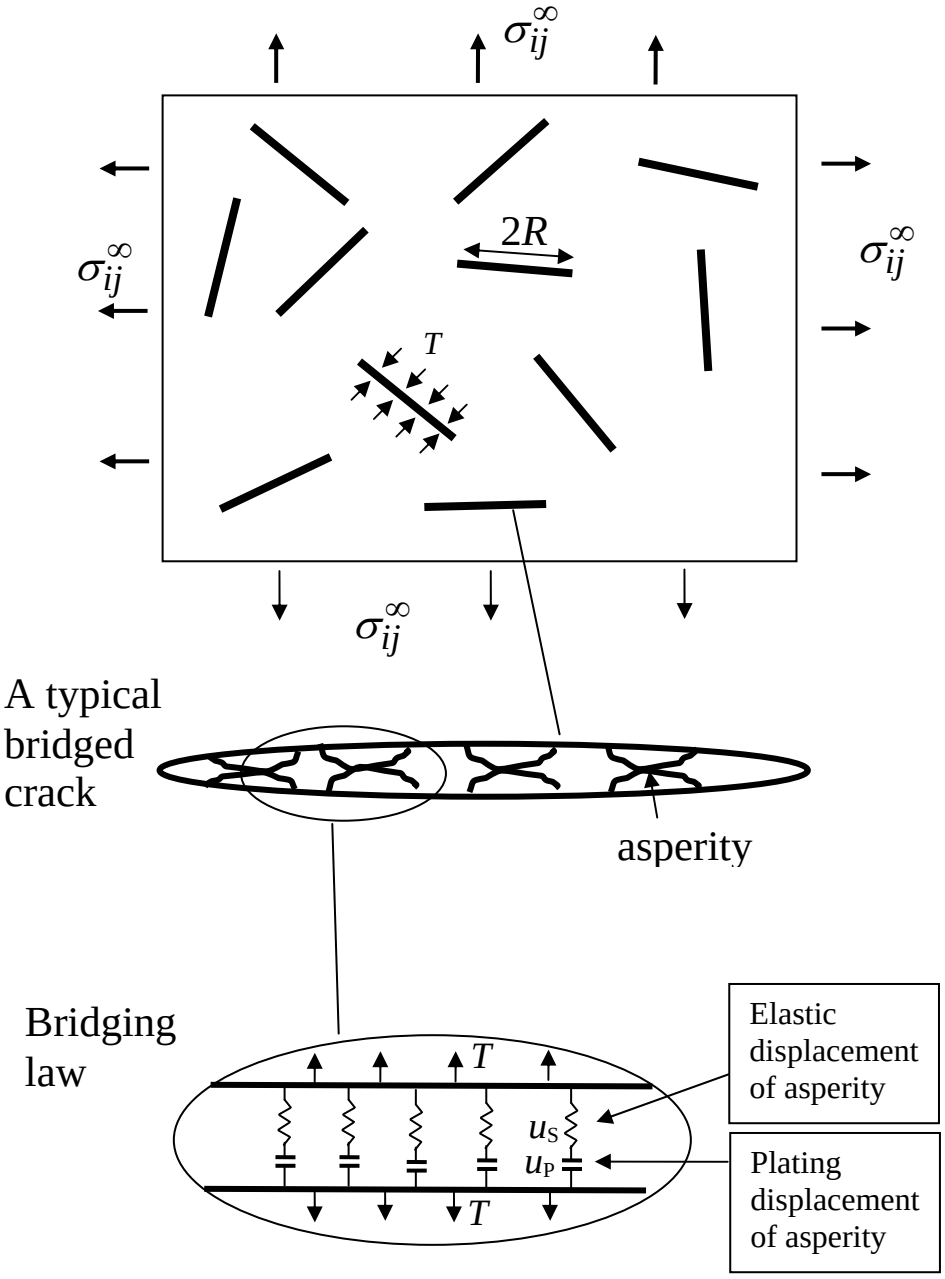

Fig. 2. The microcracked geometry under study. The matrix surrounding the penny-shaped cracks is elastic, linear viscous. A tensile traction T pulls the faces of each crack together, under the assumed sign convention. This tensile traction stretches the bridging asperities across the crack faces, as illustrated in the intermediate figure. The lower figure details the partitioning of crack bridging displacements into elastic and plating (sintering) components.

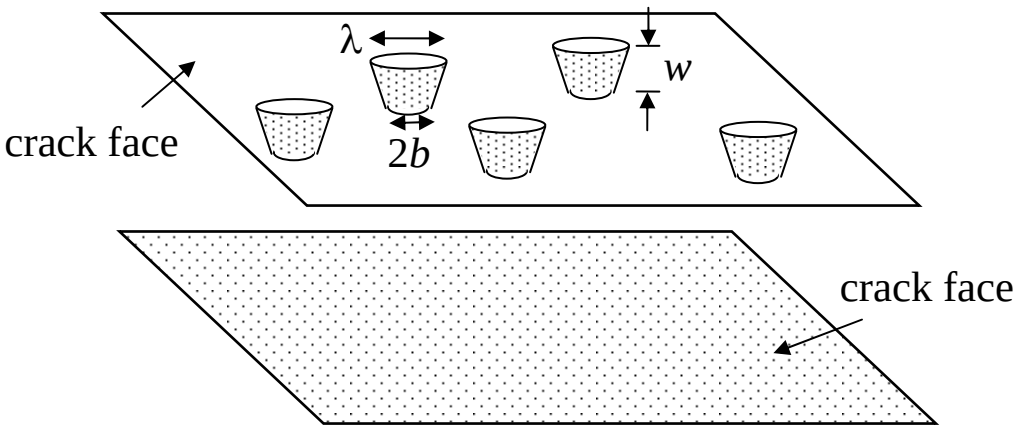

Fig. 3 Idealisation of the surface roughness on the surface of each penny shaped crack. The roughness is represented by a random distribution of conical frusta.

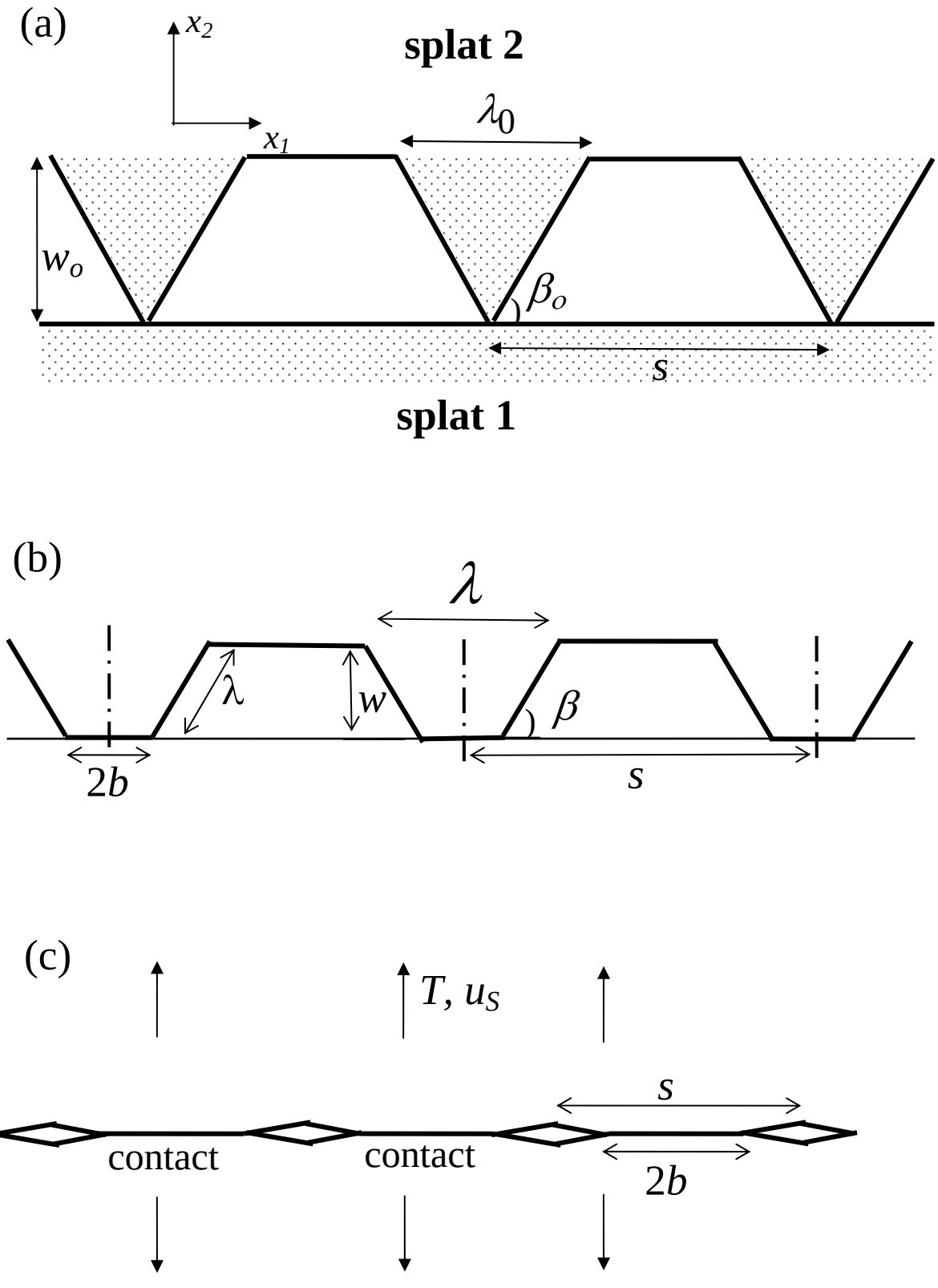

Fig. 4. The local contact geometry at asperities on the surfaces of a penny shaped crack. (a) reference configuration; (b) typical state; (c) late stage of sintering.

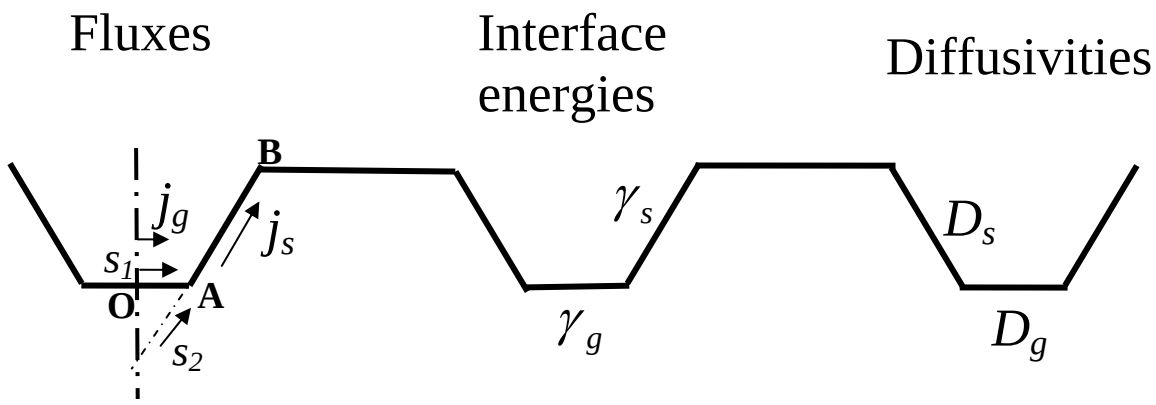

Fig. 5. Definition of fluxes, surface energies and diffusivities at the contacts.

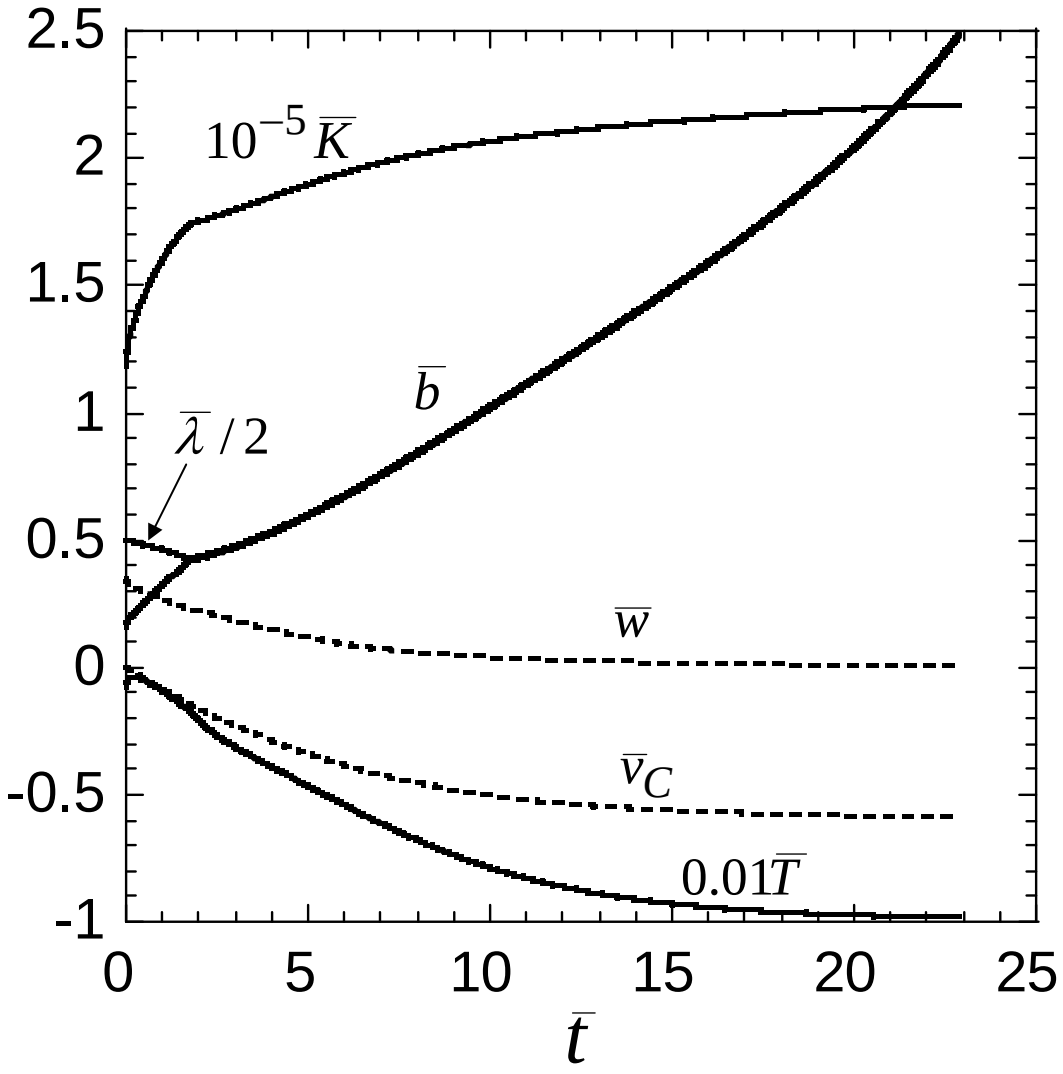

Fig. 6. HIP response for a constant applied pressure of $\bar{p} = 100$.

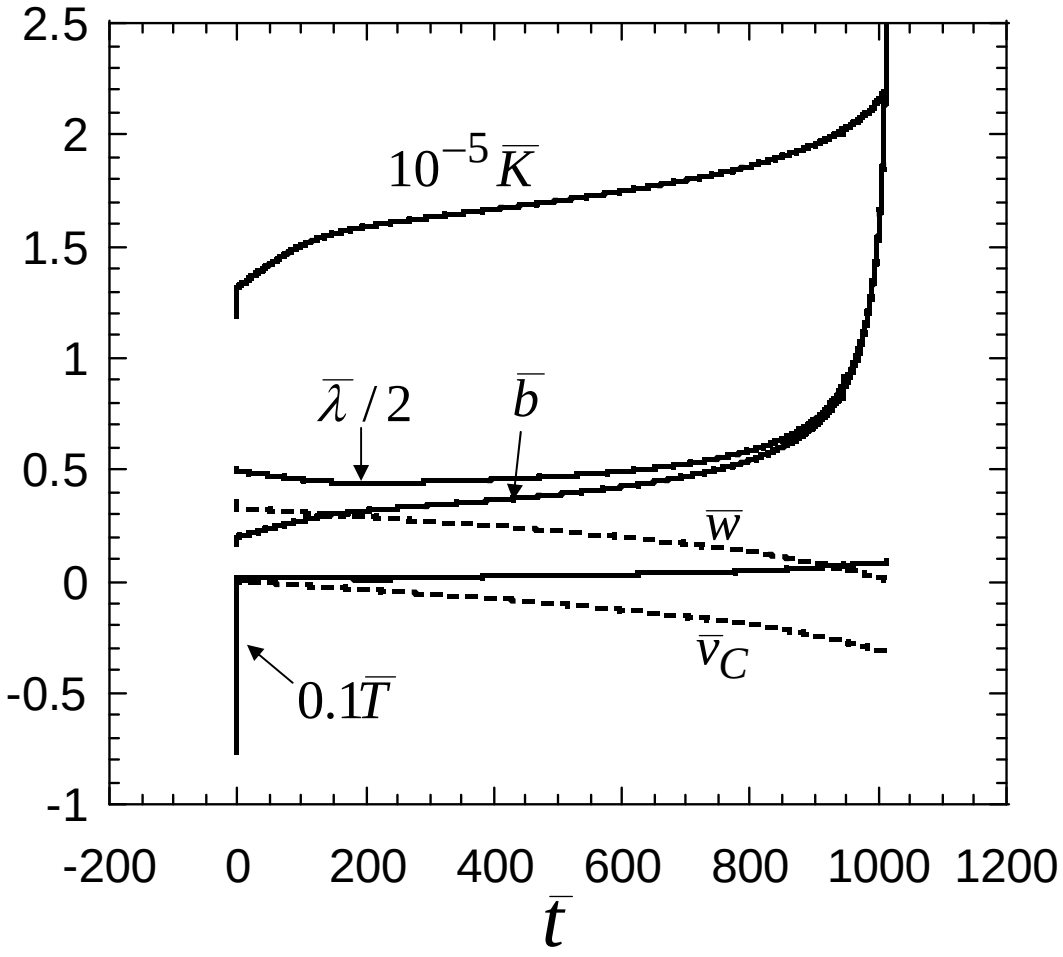

Fig. 7. Pressureless sintering response, $\overline{p}=0$.

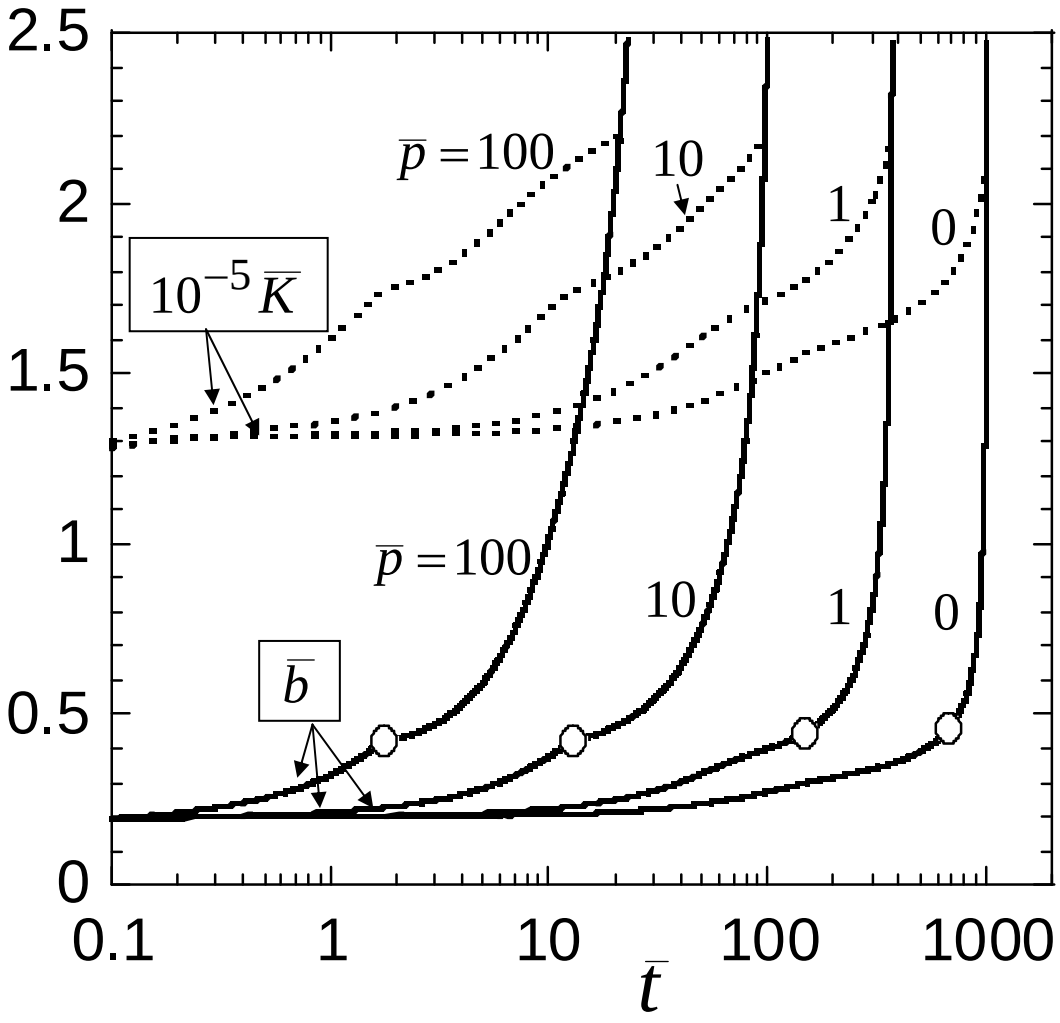

Fig. 8. Sensitivity of sintering rate and effective bulk modulus to the pressure. The open circles on the $\bar{b}$ -curves denote the point where the asperity shape has evolved from a conical frustum to a circular cylinder.

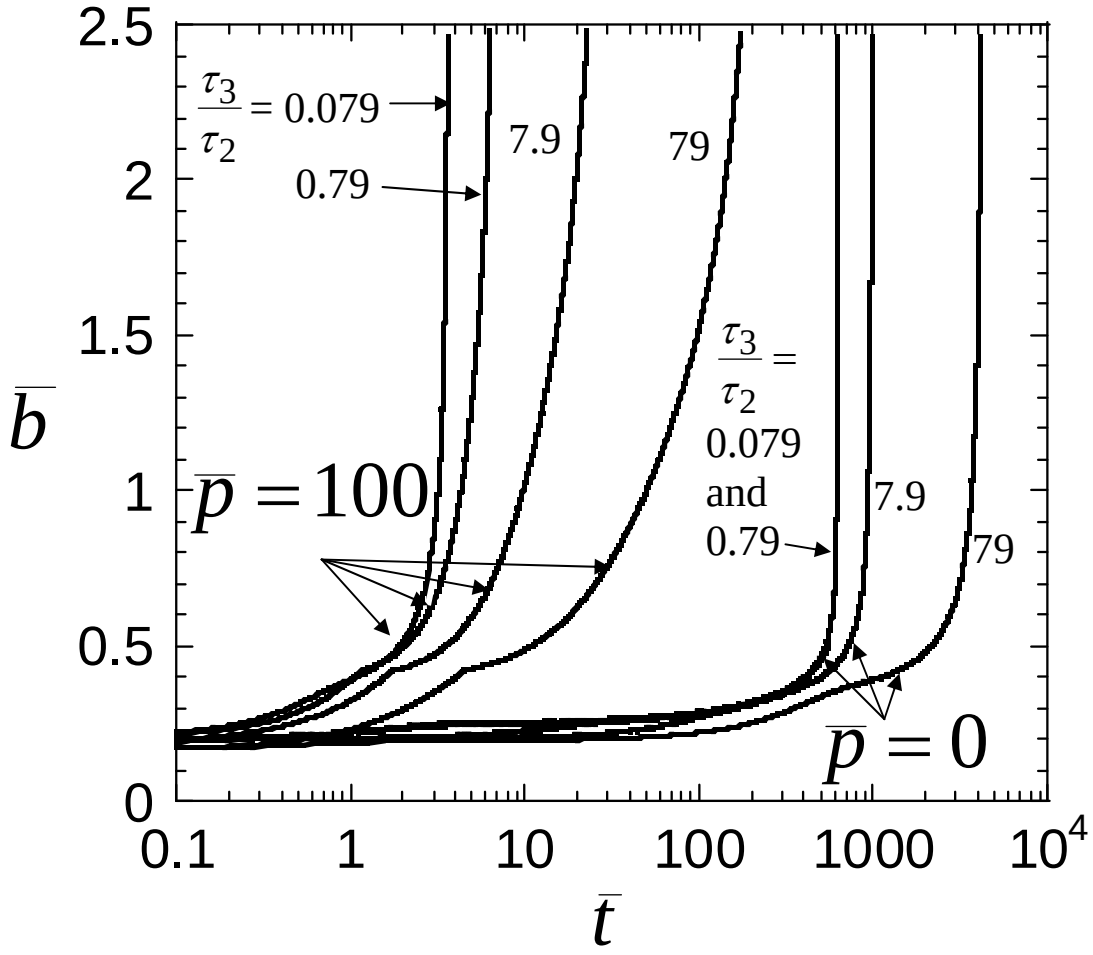

Fig. 9 Sensitivity of sintering response to τ_3 / τ_2, for $\bar{p}$ = 0, 100.